Nano Energy 94 (2022) 106898

Contents lists available at ScienceDirect

Nano Energy

journal homepage: www.elsevier.com/locate/nanoen

Highly efficient, ultrathin, Cd-free kesterite solar cells in superstrate configuration enabled by band level tuning via Ag incorporation

Zhuoran Wang [a], Yongjie Wang [a], Gerasimos Konstantatos [a,b,*]

[a] ICFO - Institut de Ciencies Fotoniques, Av. Carl Friedrich Gauss 3, Castelldefels, 08860 Barcelona, Spain
[b] ICREA-Institució Catalana de Recerca i Estudis Avancats, Passeig Lluís Companys 23, 08010, Barcelona, Spain

ARTICLE INFO

Keywords:
Kesterite solar cells
Superstrate
TiO_2
Cd-free
Silver substitution

ABSTRACT

Kesterite, or $Cu_2ZnSn(S,Se)_4$ (CZTS) is promising in developing sustainable PV technology due to its earth-abundant, non-toxic composition. However, issues including instability of interface, high density of defects that fails to allow the short charge-collection length to meet its light absorption needs, use of Cd that fails to comply with the restriction of hazardous substances (RoSH), are promoting the development of alternative, eco-friendly device structure. Here, this study reports an important progress on this subject by adopting the superstrate configuration to kesterite, thus to realize advantageous light management and high defect tolerance in an ultrathin device. By incorporating Ag in kesterite to overcome the detrimental alignment at the pristine interface, a solar cell with PCE of 8.1% has been fabricated with ~ 200 nm absorber and ~ 15 nm TiO_2 buffer, representing a PCE improvement of nearly three-fold from the baseline $Cu_2ZnSn(S,Se)_4$ device and breaking the 5% PCE limit for superstrate kesterite cells to date. Moreover, this enables the sole use of TiO_2 as novel buffer material free of toxic Cd. Further analysis reveals the critical role of Ag in synergistically tailoring band offset and bandgap, along with largely reduced density of defects, leading to this substantial performance improvement.

1. Introduction

To meet the terawatt scale needs from the solar energy market for the next decade [1], the development of earth abundant, restriction-of-hazardous-substances (RoHS)-compliant photovoltaic materials is highly important [2]. In view of this, kesterite or $Cu_2ZnSn(S,Se)_4$ (CZTS) thin film photovoltaics (TFPVs) have attracted attention in recent years [3]. A standard kesterite solar cell employs a Mo/absorber/CdS/ZnO/TCO substrate configuration [4] directly adopted from CIGS, which is however problematic because the instability of kesterite-Mo interface generates adverse secondary phases/voids that either optically or electrically compromise device performance [5-8]. Rather than simple layer insertion (e.g. Al_2O_3 [9], TiN [10], MoO_x [11], $CuGaSe_2$ [12], etc.), or replacement (Mo by FTO [13] or MoO_x/Au[14]) that only mitigate the problem, alternative device structures with completely different concept of design would be promising in fundamentally solving this issue, which has led to the recent advances in superstrate kesterite solar cells. [14].

Fig. 1a shows a schematic comparison of superstrate and substrate configurations, where the former starts from the TCO/electron transport layer (ETL) side and finishes with a high work function contact [5]. By selecting inert buffer material, morphological and phase defects at back contact can be largely reduced [13]. More importantly, the flexibility of using highly reflecting contact such as Au or MoO_x/Ag will allow advantageous light management and enable ultrathin devices (<400 nm absorber) [15]. This advantage is of particular importance in tackling the issue of mismatched optical absorption with electrical transport in conventional substrate device, that is, the inevitably formed thick non-reflecting $Mo(Se,S)_x$ layer requires ~2 μm thick absorber for efficient photon utilization which is difficult to be satisfied by the short charge-collection length in kesterite [9,15]. Additionally, the possibility of applying TCO contact on both sides can realize transparent PV modules, which is attractive in novel BIPV applications such as solar windows.

The key to enable a superstrate kesterite solar cell lies in the appropriate selection of ETL or buffer layer, which should be chemically stable under elevated temperature and S/Se rich environment, with superior n-type conductivity that can form high quality junction with kesterite. ZnO as window layer in both standard substrate CZTS and superstrate CIGS solar cells, was spontaneously adopted for superstrate kesterite device in early years [16]. However, the chemical instability during sulfurization/selenization when in contact with CZTS has limited

* Corresponding author at: ICFO - Institut de Ciencies Fotoniques, Av. Carl Friedrich Gauss 3, Castelldefels, 08860 Barcelona, Spain.
E-mail address: Gerasimos.Konstantatos@icfo.eu (G. Konstantatos).

https://doi.org/10.1016/j.nanoen.2021.106898
Received 16 September 2021; Received in revised form 23 November 2021; Accepted 27 December 2021
Available online 29 December 2021

its device efficiency to ~ 3.6% [17]. By contrast, TiO_2 is a wide bandgap, RoHS-compliant electron transport layer (ETL), with superior chemical stability [13], which could be a promising candidate. Nevertheless, the far-from-optimal interface of TiO_2 and kesterite has impeded the realization of high performance cells with reported efficiencies so far not exceeding 2% [18,19]. This has made the use of CdS indispensable to reach the-state-of-the-art 4–5% PCE for this class of kesterite solar cells [14,19]. However, the instability of CdS during selenization further limits its functionality, not to mention its parasitic light absorption and toxicity [20]. Therefore, developing an effective strategy in tailoring kesterite to match the energy levels of TiO_2 and avoiding toxic Cd becomes critical in this regard. To this end, we took the view that instead of identifying suitable intelayers between the kesterite absorber and the titania, we would aim to directly tune the energy levels of kesterite by compositional engineering, in order to form an efficient heterojunction.

Foreign cation substitution of Cu by Ag is one of the most effective strategies in tuning kesterite optical and electrical properties [21]. Except for improving film quality and reducing Cu_{Zn} antisites as commonly reported [22,23,21], another attractive but overlooked benefit of Ag substitution is that by varying the atomic ratio of Ag/(Cu+Ag), the kesterite bandgap (BG) can be largely tuned from 1.0 eV ($Cu_2ZnSnSe_4$) to 2.0 eV (Ag_2ZnSnS_4), hence the resulted high extent of availability in band positions can potentially realize the targeted match of energy levels. Therefore, in this study, by incorporating Ag into standard kesterite, we turn the detrimental "cliff" to a beneficial "spike" conduction band offset (CBO) with TiO_2 buffer layer, and fabricate a Cd-free device with 8.1% PCE– a nearly three-fold improvement from its baseline $Cu_2ZnSn(S,Se)_4$ device. A summary of the-state-of-the-art is shown in Fig. 1b and Table S1, presenting herein a new record for superstrate kesterite solar cells to the best of our knowledge.

2. Results and discussion

2.1. Superstrate solar cell construction and Ag incorporation

Fig. 1a shows the configurations of superstrate (left) and substrate (right) kesterite solar cells. The main difference lies in the fabrication sequence where the former starts from the TCO side and the latter from the Mo metal contact (both from the bottom to the top in the schematics). For superstrate devices, using a highly light-reflecting top contact (Au or Ag) permits a duplicated path of photon-to-electron conversion within the same absorber thickness, while the standard Mo substrate is non-reflective due to the formation of a thick $Mo(Se,S)_x$ [6,8] (100 nm ~1 μm) during kesterite processing. Therefore, this in principle enables thinner absorber to work efficiently in superstrate configuration [5] as depicted in the schematics. Device modeling further discloses the superiority of superstrate (Au contact) over substrate ($MoSe_x$/Mo contact) configuration, that is, allowing much thinner device (use 40% or 50% less material) to reach higher efficiency (up 20% improvement). More discussion and modeling details are provided in Section S1 in the Supporting Information (SI).

To construct the superstrate solar cell, a thin TiO_2 layer (15 nm) was at first sputtered on FTO glass, which prevents the detrimental diffusion/reaction with FTO layer as buffer and blocks holes as ETL as shown on the left of Fig. 1a. After that, a molecular ink-based solution coating followed by selenization at 490 °C was performed to fabricate kesterite active layer [24]. Then a thin layer of PTB7 (~5 nm) was spin-coated on top as hole transport layer (HTL) to tailor any morphological/surface defects before finishing with thermal evaporation of MoO_x (8 nm)/Au (100 nm). Tuning Ag/(Cu+Ag) ratio in kesterite was realized by partially replacing Cu with designated amount of Ag in precursor solution, and the corresponding film/device is named as Ag X% for simplicity where X is the atomic ratio of Ag/(Cu+Ag). The obtained films were characterized by Raman, SEM, and XPS as discussed in Section S2-S5 (SI), respectively, confirming the purity of selenized kesterite phase, successful Ag incorporation, and the importance of controlled Ag fraction in leading to smoother and larger grains while avoiding morphological distortion. Moreover, XPS provides a direct access to the valence band maximum (VBM) and Fermi level energy (E_F)[25] that are summarized in Table 1. It shows that as Ag ratio increases, E_F moves away from the VBM, indicating the decrease of p-type conductivity as previously reported [22].

Photovoltaic performance of kesterite superstrate devices from different Ag X% precursors were evaluated at standard testing conditions. Similar to previous study, $Cu_2ZnSn(S,Se)_4$ (Ag 0%) superstrate devices demonstrate barely 2% PCE in average (Fig. 2a) [26]. By contrast, Ag substitution substantially improves the situation: with the optimal atomic ratio set to Ag/(Cu+Ag) = 30% in precursor solution, the fabricated devices yield an average PCE of over 7%, representing over 250% improvement from the unsubstituted device (Ag 0%). J-V characteristics of the best devices in Ag 0%, Ag 30%, and Ag 50% groups are plotted in Fig. 3b with the extracted figures of merit shown in Table 2. The champion device from the Ag 30% group generates the record PCE of 8.1%, which is also the first report on TiO_2 as RoHS-compliant buffer/ETL in kesterite device that shows competitive performance to the other Cd-free buffer materials (e.g. ZnSnO [27,28], Zn(O,S) [29], In_2S_3 [30], etc.), thus it is particularly important in

Table 1
VBM and E_F extracted from XPS measurement.

	Ag 0%	Ag 30%	Ag 50%	TiO_2
E_F-VBM (eV)	0.36	0.55	0.66	2.76
E_F (eV vs Vacuum)	4.17	4.28	4.23	4.01

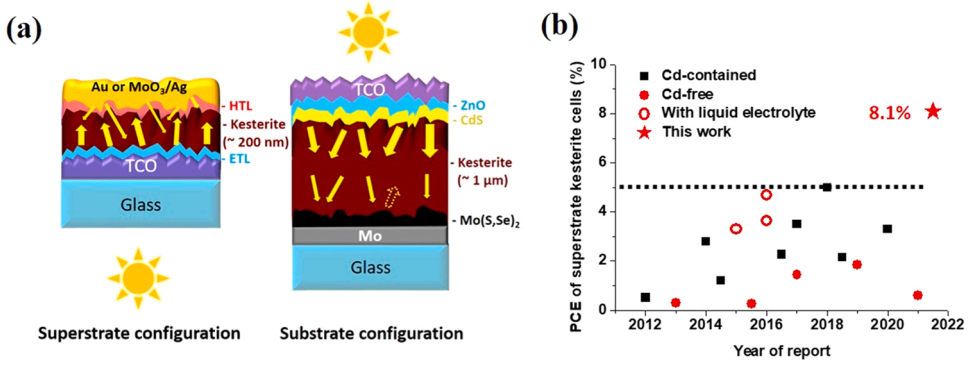

Fig. 1. (a) Device configuration of superstrate vs substrate kesterite solar cells (ETL- electron transport layer; HTL- hole transport layer); (b) Plots of the state of the arts of superstrate kesterite solar cells with details listed in Table S1 in SI, where the dash line marked the record of 5% PCE to date and the star symbol represents the result of this work.

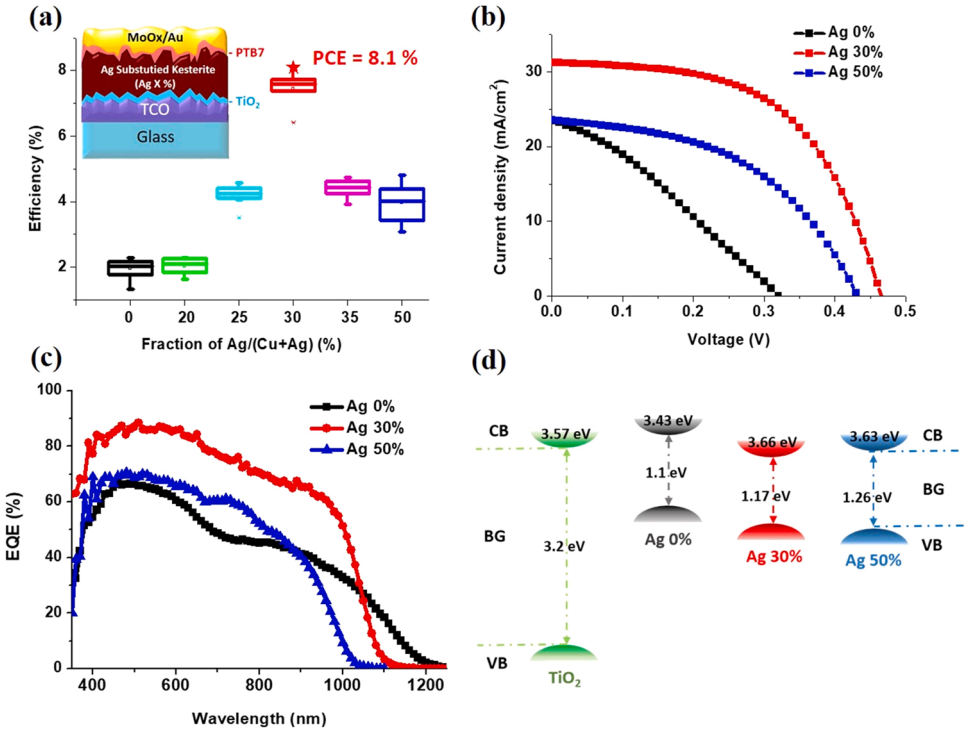

Fig. 2. (a) Efficiency statistics of superstrate solar cells with Ag(Cu+Ag) fraction from 0% to 50% where the star symbol represents the champion device and inset shows the device configuration; (b) J-V characteristics of best cell within Ag 0%, Ag 30%, and Ag 50% groups; (c) the corresponding external quantum efficiency (EQE) spectra and (b) measured energy band positions in reference to TiO_2.

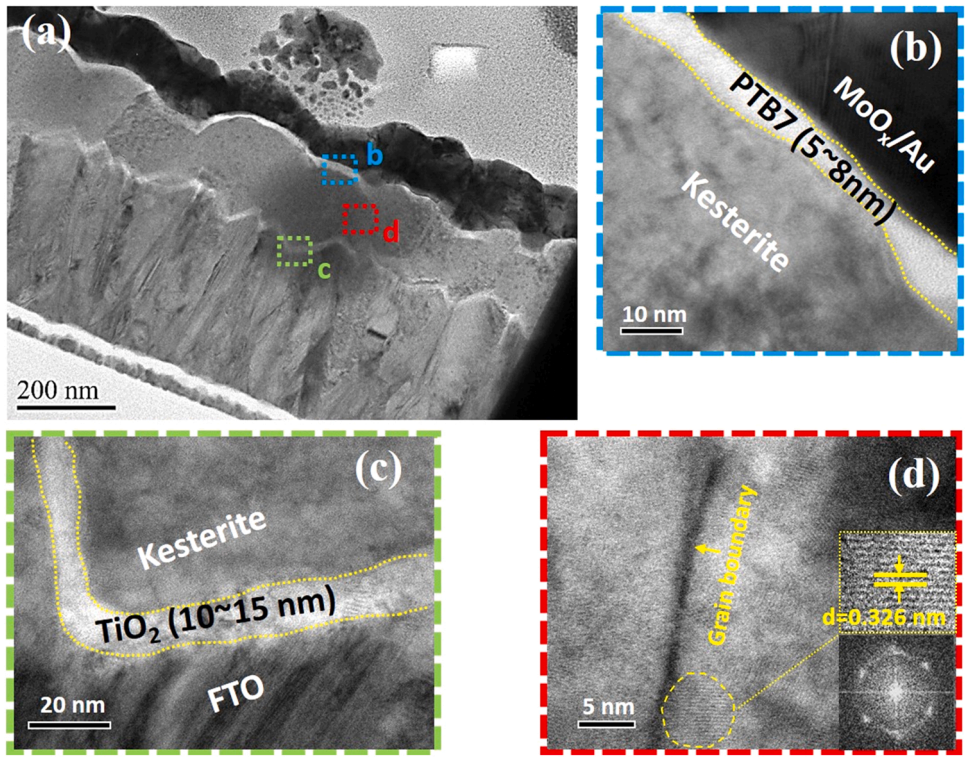

Fig. 3. (a) Low-magnification TEM image of device cross-section; (b) HRTEM image at top, (c) bottom interface, and (d) grain-boundary area within the kesterite layer where the insets show the corresponding Fast Fourier transform (FFT) pattern and magnified nano-grain region (circled).

developing fully-sustainable PV technologies. The boosted PCE, therefore, shows that adding Ag is critical in the kesterite-TiO_2 device system. However, further increasing Ag content to 50% does not result in better efficiency, which is likely due to the morphological distortion (i.e. cracks) as shown in Fig. S3e&f (SI). In addition, the altered electrical properties (p-type conductive to intrinsic) [22] with high Ag content

Table 2
Figures of merit of champion devices with different Ag/(Cu+Ag) ratio.

Device ID	η (%)	J_{sc} (mA/cm^2)	V_{oc} (V)	FF	E_g (eV)	E_u (meV)	$CBM_{Ag\ x\%}$ - CBM_{TiO2}
Ag 0%	2.3	23.4	0.32	0.30	1.10	25.4	- 0.14 ("cliff")
Ag 30%	8.1	31.2	0.47	0.55	1.17	23.7	+ 0.09 ("spike")
Ag 50%	4.8	23.7	0.42	0.48	1.26	21.3	+ 0.06 ("spike")

may require additional efforts on device optimization [31]. Therefore, at this stage, we consider Ag 30% an optimal condition for Ag substitution, upon which we focus in the following discussion.

Fig. 2c shows their corresponding EQE spectra. Apart from the improved EQE in the visible range (over 80% for Ag 30%), Ag substitution has also changed the spectral profiles. By plotting $[Eln(1\text{-}EQE)]^2$ versus photon energy (E) and linearly fitting the low-energy edge, as shown in Fig. S6a (SI), bandgap (BG) of 1.1 eV, 1.17 eV, 1.26 eV was extracted for Ag 0%, Ag 30%, Ag 50%, respectively, showing that Ag substitution is enlarging the bandgap (BG) of kesterite. Further, Urbach analysis was performed in Section S6 (SI) to evaluate their band tailing behaviors [32]. As the Ag ratio increases, Urbach tail energy (E_u) decreases accordingly from 25.5 meV (Ag 0%) to 23.7 meV (Ag 30%) or 21.3 meV (Ag 50%), indicating the regulated band tailing, which may correlate to reduced Cu_{Zn} antisites upon Ag substitution. Moreover, by referring to the measured VBMs and BGs, a full picture of band positions is reconstructed in Fig. 2d. Ag incorporation brings down the conduction band maximum (CBM) and change the initial "cliff" ($CBM_{kesterite} - CBM_{TiO2} < 0$) conduction band offset (CBO) for Ag 0% to a small "spike" for either Ag 30% or Ag 50%, which is generally a beneficial situation for TFPVs [20] as discussed in Section S7 (SI). Therefore, the improved PCE in Ag-substituted kesterite absorbers stems from the regulation of the band-offset position forming a favorable junction profile. This topic will be further discussed via in-depth device characterization in Section 2.3.

2.2. Nanoscale characterization of thin film and device

To gain insights on the device structure, a cross-section lamella was prepared by focused ion beam (FIB) on the champion device (Ag 30%) and characterized by TEM. The absorber showed a thickness of ~200 nm with considerable roughness (Fig. 3a), on the sides of which, the continuities of PTB7 and TiO_2 are confirmed and the estimated thickness is 5–8 nm (Fig. 3b) and 10–15 nm (Fig. 3c), respectively. Grain boundaries can be clearly seen in Fig. 3d where each of these short grains (~ 200 nm in height) demonstrates polycrystalline feature (ring-shaped FFT pattern as inset) instead of a single crystal. In fact, nano-grains can be seen in the image. For example, a nanoparticle of ~8 nm in diameter shows d-spacing of 0.326 nm, which corresponds to kesterite (112) plane. The compositional uniformity at nanoscale was also proven by EDS maps and line scan in Fig. S8 (SI), where the intact preservation of TiO_2 buffer after kesterite processing is also confirmed. More importantly, the detrimental voids that were commonly seen when interfacing with Mo or FTO substrate are absent in this study, showing an improved interface by using TiO_2 buffer layer. Additionally, abnormally large grains with height of ~400 nm is seen to appear occasionally (Fig. S9 in SI), which results from of an intermediate stage of liquid-phase-involved crystal growth [33] as discussed in Section S3&S4 (SI).

2.3. The origin of Ag-boosted PCE

To elucidate the role of Ag in improving the solar cell performance, in-depth device characterization was carried out aiming at gaining insights on defects and transport characteristics of the Ag-substituted films. Fig. 4a shows the results of capacitance-voltage (C-V) and drive level capacitance profiling (DLCP) measurement at room temperature. Ag substitution resulted in one-order-of-magnitude lower intrinsic carrier densities (10^{16} to 10^{15} cm^{-3} from N_{DLCP} at 0 V bias marked with dash lines), in agreement with the increased E_F – VBM value from the

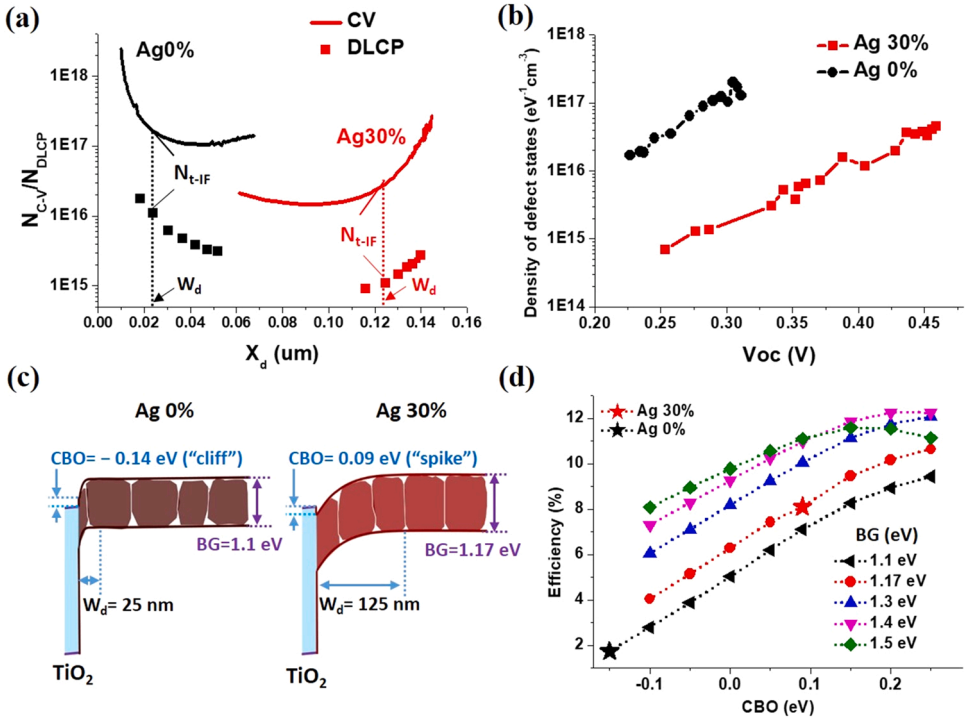

Fig. 4. (a) C-V and DLCP measurement of charge carrier density; (b) density of defect states extraction from photovoltage/photocurrent transient (TPV/TPC) measurement; (c) schematics of interface band diagram of Ag 0% and Ag 30% devices at zero bias; (d) conduction band offset (CBO) dependent solar cell efficiency of absorber with varied bandgap (BG) via numerical modeling, where star symbols represent the conditions of Ag 0% and Ag 30% from experiment.

XPS measurement. The substantial difference between $N_{C\text{-}V}$ and N_{DLCP} also points to high densities of interfacial defects ($N_{t\text{-}IF}$) in both devices [4,34]. The one-order-higher value of $N_{C\text{-}V} - N_{DLCP}$ in Ag 0% (10^{17} cm^{-3} vs 10^{16} cm^{-3}) indicates a more severe interface recombination. In addition, depleted region width (W_d) is significantly widened from 25 nm to 125 nm after Ag substitution, which thus contributes to better charge collection in Ag 30% device. To further probe the charge transport characteristics in Ag 30%, photo-induced charge carrier extraction by linearly increasing voltage (Photo-CELIV) [35], were applied for carrier mobility extraction, with details shown in Fig. S11 (SI). The measurements yield a mobility (μ) of 0.02 cm^2/Vs. The rather low mobility of our films is considered due to the nano-crystallinity of kesterite demonstrated in Fig. 3 as compared to a layer of closely attached sub-microcrystals within the standard thick kesterite devices (with reported μ = 1–100 cm^2/V.s) [22,36].

Transient photovoltage/photocurrent was then applied (TPV/TPC) to probe the lifetime and defects profile with details provided in Section S12 [37,38]. Based on this analysis, Fig. 4b shows an over one-order-lower defect density upon Ag introduction. This reduction could be due to the reduced amount of antisite defects as the formation energy of Ag_{Zn} is much higher than Cu_{Zn} [39], which also resulted in moderately enhanced TPV lifetime as shown in Fig. S12c. Thermal admittance spectroscopy thus assisted to explore further in this regard and discussed in Section S13 (SI) [40,23,41]. An activation energy of 0.12 eV attributing to Cu_{Zn} antisites ($N_t = 2 \times 10^{17}$ cm^{-3}) was identified in Ag 0%, while this defect is absent in Ag 30%. Therefore, Ag substitution has contributed to substantially reducing Cu_{Zn} antisites as expected. However, the still considerable bulk (2×10^{15} cm^{-3} integrated from TPV/TPC) and interface defects ($N_{t\text{-}IF} = (N_{C\text{-}V} - N_{DLCP}) \times W_d = 3 \times 10^{11}$ cm^{-2}) could be the origin of the PCE limit in the current champion device (Ag 30%).

Based on the measured optoelectronic characteristics (e.g. CBO, BG, absorbance, μ, carrier and defect densities, etc.), extended discussion of the TiO_2-kesterite (Ag alloyed) superstrate device was carried out assisted by numerical modeling. Technical details are provided in Table S3 (SI). Fig. 4c reproduces the simulated band diagrams, depicting that incorporation of Ag modifies CBO from a − 0.14 eV "cliff" to a 0.09 eV "spike" for absorbers with bandgap (BG) of 1.1 eV (Ag 0%) and 1.17 eV (Ag 30%), respectively. The narrowed distance from CBM_{TiO2} to $VBM_{kesterite}$ in Ag 0% is suspected to cause severe cross-band recombination and limit PCE, which is then validated via simulation in Fig. 4d. At first, a simulated PCE of 8.1% is obtained by using measured parameters of Ag 30% showing J_{sc}, V_{oc}, FF, identical to the experimental data (Section S15 in SI), which is thus considered a valid baseline (red star symbol in Fig. 4d). Then, in order to mimic the fact that Ag substitution tends to affect CBO and BG simultaneously [22], the synergistic effects of both parameters were probed. As expected, a moderate "spike" alignment is beneficial to the device efficiency in all conditions. Moreover, the combination of a 0.1–0.25 eV "spike" and a wider BG (1.3 or 1.4 eV) leads to the highest efficiency of over 12%, while a small "cliff" of beyond − 0.1 eV with 1.1 eV BG absorber substantially reduces its PCE to barely 2%, which well correlates to the case of Ag 0% device (black star symbol). The result therefore points out the dominant impact of CBO&BG, as they are the only variables in this modeling but critical enough to reproduce the nearly three-fold PCE boost observed in experiment. Moreover, this also provides insights for improvement, as according to Fig. 2d, increasing the fraction of Ag to 50% further widened its BG to 1.26 eV without much influenced CBO, which is closer to the optimal condition predicted by Fig. 4d. Thus, it is rational to expect further PCE improvements by developing kesterites with higher Ag fraction provided the morphology/phase could be well controlled. Additionally, wide ranges of thickness, N_A, Nt, are also probed to gain well-rounded knowledge as well as to exclude any uncertainty from the measurement/estimation, which provides insights for further device optimization including light trapping design and interface passivation [42] as explicitly discussed in Section S15 (SI).

In summary, the boosted PCE in this study is mainly attributed to the Ag-tailored band alignment at the interface, along with the reduced defects. It further suggests the importance in synergistically tuning CBO/BG/N_A, as well as tackling interfacial defect for achieving higher solar cell efficiency.

3. Conclusion

Herein, a Cd-free, kesterite solar cell in superstrate configuration was fabricated and 8.1% PCE was achieved, having benefited from the demonstrated advantage of superstrate configuration over standard substrate structure: reduced material utilization and improved defect tolerance. Silver substitution in kesterite has significantly improved solar cell performance, which is attributed to the tailored CBO (from detrimental "cliff" to beneficial "spike") and suppressed defects. A thin layer of TiO_2 (10–15 nm) was used as buffer/ETL to have eliminated the use of Cd and overcome the instability of standard kesterite/Mo interface. Cross-sectional TEM revealed the polycrystallinity of the kesterite film consisting of nano-grains, which resulted in the low mobility of 0.02 cm^2/V.s. Thus, better controlling of the liquid-phase formation and crystal growth is proposed to improve the carrier transport in this Ag-alloyed kesterite system. The device defect characteristics was further probed, where Ag contributes to eliminating Cu_{Zn} antisite defects. At the end, importance in synergistically tuning CBO/BG and tackling interfacial defects were identified, which are promising paths towards technically competitive level for kesterite superstrate solar cells.

4. Methods

4.1. Preparation of Ag substituted kesterite thin film

Kesterite thin film was deposited on substrate by multi-layers of spin-coating precursor solution. The precursor solution or "molecular ink" was prepared by dissolving copper acetate $Cu(CH_3COO)_2$ (0.44 M), zinc chloride $ZnCl_2$ (0.28 M), tin chloride dihydrate $SnCl_2.2H_2O$ (0.23 M), and thiourea CH_4N_2S (1.54 M) in Dimethylformamide (DMF) at room temperature. For Ag substitution, a separate precursor solution was prepared containing silver chloride AgCl (0.44 M) instead of copper acetate while the other chemicals remained the same. Designated amount of Ag precursor was directly mixed with Cu precursor to realize convenient tuning of Ag/(Cu+Ag) ratio. After that, the mixed solution was spin-coated at 3000 RPM for 1 min and baked on a hotplate at 200 °C for 3.5 min, which was repeated for three times to obtain required thickness of the precursor film (~ 300 nm). Then selenization was performed on the obtained precursor film within a compact rapid thermal process (RTP) chamber (MTI Corp.) at 490 °C for 16 min protected by Ar which was then slowly cooled down to room temperature in 4 h. Excess selenium pellets were loaded in the graphite box during the process. The base pressure was set to 450 Torr and Se consumption rate was estimated to be 4 mg/min.

4.2. Solar cell device fabrication

At first, 15 nm TiO_2 buffer layer was deposited on cleaned FTO glass (TEC 15, Sigma Aldrich) by RF sputtering at 150 W, 2 mTorr chamber pressure with Ar. The deposition rate was calibrated to be 0.75 nm/min. Then the as-prepared TiO_2 substrate was placed on a 200 °C hotplate for 15 min, which was followed by UV-Ozone treatment for 10 min. Kesterite deposition and selenization were directly applied on the TiO_2 layer afterwards. Subsequently, an ammonium sulfide solution cleaning procedure was followed for passivation and removal of any Cu/Sn selenide secondary phase on the surface, which is considered a benign alternative to KCN. PTB7 (5 mg/mL in 1,2-Dichlorobenzene, Ossila) as HTL was then spin-coated at 3000 RPM, before finally finishing with thermal evaporated MoO_x (8 nm) and Au (100 nm) contact.

4.3. Material characterization

Light absorption spectroscopy of thin film was performed with Cary 5000 UV–VIS–NIR spectrometer. Raman spectroscopy was performed with Renishaw Raman system with excitation wavelength of 514 nm. SEM measurement was carried out with the FEI Inspect F50 system with accelerating voltage of 5 KV. Cross-section lamella was prepared with FESEM-FIB system (FEI Scios 2), which was then characterized by TEM (JEOL 2100) operating at an accelerating voltage of 200 kV. XPS was performed with a Phoibos 150 analyser (SPECS) in ultrahigh-vacuum conditions (base pressure of 1×10^{-10} mbar) with a monochromatic Kα X-ray source (1486.7 eV). The determination of fermi level of semiconductor was realized by applying 10 V bias to eliminate the influence from the detector, which was subtracted for the calculation.

4.4. Device characterization

The current–voltage measurements were performed with a Keithley 2400 source meter and a calibrated Newport Oriel Sol3A solar simulator (AM 1.5 G) under ambient conditions. The EQE was measured using a Newport Cornerstone 260 monochromator, a Thorlabs MC2000 chopper, a Stanford Research SR570 trans-impedance amplifier and a Stanford Research SR830 lock-in amplifier. A calibrated Newport 818-UV photodetector was used as a reference. The capacitance–voltage (C–V) measurement was performed with Agilent B1500A semiconductor analyzer connected to an external capacitance measurement unit. The AC bias voltage amplitude was set at 50 mV with frequency 100 kHz. The acquired C–V data were processed with Mott–Schottky analysis for determining charge density ($N_{c\text{-}v}$) and depletion width at zero bias. With the same step up, drive level capacitance profiling (DLCP) measurement was performed but under various AC bias amplitude of 20–250 mV at each profiling depth. Transient photovoltage/ photocurrent (TPV/TPC) measurements were performed with an Agilent 4000X oscilloscope using a 1 MΩ (50 Ω) input terminal and a Vortran Stradus laser with a wavelength of 637 nm. A FiberTech Optica LED light source provided the bias light. A function generator was used to control the laser, with a frequency of 10 Hz and pulse width of 100 μs. The intensity of the laser was adjusted to keep the voltage transient amplitude under 5% of the steady state light bias. Carrier lifetime τ was determined by fitting the exponential V_{oc} decay at 1 Sun. The in-gap density of states was calculated by combining the TPV and TPC data. The TPC curve was integrated to get the charge generated (ΔQ) in the devices due to the laser pulse. The capacitance (C) was calculated from the $C = \Delta Q/\Delta V_{OC}$ relation. The total charge carrier was calculated from the integration of C versus V_{OC} plot. Charge carrier density was calculated by dividing the total charge carriers with the device volume. Thermal admittance spectroscopy (TAS) measurements were performed with the PV devices in a Lakeshore four-probe cryogenic chamber controlled by a Lakeshore-360 temperature controller cooled by liquid nitrogen, which was connected with an Agilent B1500 for C-f measurement at zero bias. Details of data analysis of TPV/TPC, C-V, DLCP, and TAS can be found in SI.

CRediT authorship contribution statement

Zhuoran Wang: conceptualization, investigation, writing, **Yongjie Wang**: investigation, Gerasimos Konstantatos: conceptualization, supervision, writing.

Declaration of Competing Interest

The authors declare that they have no known competing financial interests or personal relationships that could have appeared to influence the work reported in this paper.

Acknowledgments

The authors acknowledge financial support from the European Research Council (ERC) under the European Union's Horizon 2020 research and innovation programme (grant agreement no. 725165) as well as from the European Union's Horizon 2020 research and innovation programme under the Marie Skłodowska-Curie grant agreement No 754558. This project has received funding also from the Spanish State Research Agency, through the "Severo Ochoa" Center of Excellence CEX2019-000910-S, the CERCA Programme / Generalitat de Catalunya and Fundació Mir-Puig. We also acknowledge Funding by the Fundació Joan Ribas Araquistain (FJRA). This project was funded also by EQC2019-005797-P (AEI/FEDER UE). Zhuoran Wang acknowledges the support from the Marie Sklodowska-Curie Individual Fellowship (SUSNASOL, grant agreement No. 886953).

Appendix A. Supporting information

Supplementary data associated with this article can be found in the online version at doi:10.1016/j.nanoen.2021.106898.

References

[1] N.M. Haegel, H. Atwater, T. Barnes, C. Breyer, A. Burrell, Y.-M. Chiang, S. De Wolf, B. Dimmler, D. Feldman, S. Glunz, J.C. Goldschmidt, D. Hochschild, R. Inzunza, I. Kaizuka, B. Kroposki, S. Kurtz, S. Leu, R. Margolis, K. Matsubara, A. Metz, W. K. Metzger, M. Morjaria, S. Niki, S. Nowak, I.M. Peters, S. Philipps, T. Reindl, A. Richter, D. Rose, K. Sakurai, R. Schlatmann, M. Shikano, W. Sinke, R. Sinton, B. J. Stanbery, M. Topic, W. Tumas, Y. Ueda, J. van de Lagemaat, P. Verlinden, M. Vetter, E. Warren, M. Werner, M. Yamaguchi, A.W. Bett, Science 364 (2019) 836.
[2] A. Wang, N.L. Chang, K. Sun, C. Xue, R.J. Egan, J. Li, C. Yan, J. Huang, H. Rong, C. Ramsden, X. Hao, Sustain. Energy Fuels 5 (2021) 1044–1058.
[3] S.K. Wallace, D.B. Mitzi, A. Walsh, ACS Energy Lett. 2 (2017) 776–779.
[4] W. Wang, M.T. Winkler, O. Gunawan, T. Gokmen, T.K. Todorov, Y. Zhu, D.B. Mitzi, Adv. Energy Mater. (2013), 2004313.
[5] M.D. Heinemann, F. Ruske, D. Greiner, A.R. Jeong, M. Rusu, B. Rech, R. Schlatmann, C.A. Kaufmann, Sol. Energy Mater. Sol. Cells 150 (2016) 76–81.
[6] V. Karade, A. Lokhande, P. Babar, M.G. Gang, M. Suryawanshi, P. Patil, J.H. Kim, Sol. Energy Mater. Sol. Cells 200 (2019), 109911.
[7] X. Liu, Y. Feng, H. Cui, F. Liu, X. Hao, G. Conibeer, D.B. Mitzi, M. Green, Prog. Photovolt. Res. Appl. 24 (2016) 879–898.
[8] C. Platzer-Björkman, N. Barreau, M. Bär, L. Choubrac, L. Grenet, J. Heo, T. Kubart, A. Mittiga, Y. Sanchez, J. Scragg, S. Sinha, M. Valentini, J. Phys. Energy 1 (2019), 044005.
[9] F. Liu, J. Huang, K. Sun, C. Yan, Y. Shen, J. Park, A. Pu, F. Zhou, X. Liu, J.A. Stride, M.A. Green, X. Hao, NPG Asia Mater. 9 (2017) e401-e401.
[10] B. Shin, Y. Zhu, N.A. Bojarczuk, S. Jay Chey, S. Guha, Appl. Phys. Lett. 101 (2012), 053903.
[11] Q. Yu, J. Shi, L. Guo, B. Duan, Y. Luo, H. Wu, D. Li, Q. Meng, Nano Energy 76 (2020), 105042.
[12] S. Giraldo, R. Fonoll-Rubio, Z. Jehl Li-Kao, Y. Sánchez, L. Calvo-Barrio, V. Izquierdo-Roca, A. Pérez-Rodríguez, E. Saucedo, Prog. Photovolt. Res. Appl. 29 (2021) 334–343.
[13] I. Becerril-Romero, D. Sylla, M. Placidi, Y. Sánchez, J. Andrade-Arvizu, V. Izquierdo-Roca, M. Guc, A. Pérez-Rodríguez, S. Grini, L. Vines, B. Pusay, R. Almache, J. Puigdollers, P. Pistor, E. Saucedo, M. Espíndola-Rodríguez, ACS Appl. Mater. Interfaces 12 (2020) 33656–33669.
[14] Z. Wang, N. Brodusch, R. Gauvin, G.P. Demopoulos, Nano Energy 53 (2018) 130–134.
[15] I. Massiot, A. Cattoni, S. Collin, Nat. Energy 5 (2020) 959–972.
[16] L. Dongwook, Y. Kijung, Nanotechnology 25 (2014), 065401.
[17] A. Ghosh, R. Thangavel, A. Gupta, J. Alloy. Compd. 694 (2017) 394–400.
[18] Z. Wang, R. Gauvin, G.P. Demopoulos, Nanoscale 9 (2017) 7650–7665.
[19] Z. Wang, N. Brodusch, R. Gauvin, G.P. Demopoulos, J. Mater. Chem. A 6 (2018) 11507–11520.
[20] A. Crovetto, O. Hansen, Sol. Energy Mater. Sol. Cells 169 (2017) 177–194.
[21] J. Li, D. Wang, X. Li, Y. Zeng, Y. Zhang, Adv. Sci. 5 (2018), 1700744.
[22] T. Gershon, Y.S. Lee, P. Antunez, R. Mankad, S. Singh, D. Bishop, O. Gunawan, M. Hopstaken, R. Haight, Adv. Energy Mater. 6 (2016), 1502468.
[23] W.-C. Huang, S.-Y. Wei, C.-H. Cai, W.-H. Ho, C.-H. Lai, J. Mater. Chem. A 6 (2018) 15170–15181.
[24] J.A. Clark, A. Murray, J.-m Lee, T.S. Autrey, A.D. Collord, H.W. Hillhouse, J. Am. Chem. Soc. 141 (2019) 298–308.
[25] M.G. Helander, M.T. Greiner, Z.B. Wang, W.M. Tang, Z.H. Lu, J. Vac. Sci. Technol. A 29 (2011), 011019.
[26] Z. Wang, N. Brodusch, R. Gauvin, G.P. Demopoulos, ACS Sustain. Chem. Eng. 7 (2019) 15093–15101.

[27] X. Cui, K. Sun, J. Huang, J.S. Yun, C.-Y. Lee, C. Yan, H. Sun, Y. Zhang, C. Xue, K. Eder, L. Yang, J.M. Cairney, J. Seidel, N.J. Ekins-Daukes, M. Green, B. Hoex, X. Hao, Energy Environ. Sci. 12 (2019) 2751–2764.
[28] L. Grenet, F. Emieux, J. Andrade-Arvizu, E. De Vito, G. Lorin, Y. Sánchez, E. Saucedo, F. Roux, ACS Appl. Energy Mater. 3 (2020) 1883–1891.
[29] J. Li, X. Liu, W. Liu, L. Wu, B. Ge, S. Lin, S. Gao, Z. Zhou, F. Liu, Y. Sun, J. Ao, H. Zhu, Y. Mai, Y. Zhang, Sol. RRL 1 (2017), 1700075.
[30] D.A.R. Barkhouse, R. Haight, N. Sakai, H. Hiroi, H. Sugimoto, D.B. Mitzi, Appl. Phys. Lett. 100 (2012), 193904.
[31] T. Gershon, K. Sardashti, O. Gunawan, R. Mankad, S. Singh, Y.S. Lee, J.A. Ott, A. Kummel, R. Haight, Adv. Energy Mater. 6 (2016), 1601182.
[32] S. Pradhan, A. Stavrinadis, S. Gupta, Y. Bi, F. Di Stasio, G. Konstantatos, Small 13 (2017), 1700598.
[33] S.-Y. Kim, D.-H. Son, S.-H. Kim, Y.-I. Kim, S. Kim, K. Ahn, K.-J. Yang, J.-K. Kang, D.-H. Kim, Adv. Energy Mater. 10 (2020), 1903173.
[34] J.T. Heath, J.D. Cohen, W.N. Shafarman, J. Appl. Phys. 95 (2004) 1000–1010.
[35] M. Stephen, K. Genevičius, G. Juška, K. Arlauskas, R.C. Hiorns, Polym. Int. 66 (2017) 13–25.
[36] T. Gokmen, O. Gunawan, D.B. Mitzi, J. Appl. Phys. 114 (2013), 114511.
[37] Y. Bi, S. Pradhan, S. Gupta, M.Z. Akgul, A. Stavrinadis, G. Konstantatos, Adv. Mater. 30 (2018), 1704928.
[38] A.H. Ip, S.M. Thon, S. Hoogland, O. Voznyy, D. Zhitomirsky, R. Debnath, L. Levina, L.R. Rollny, G.H. Carey, A. Fischer, K.W. Kemp, I.J. Kramer, Z. Ning, A.J. Labelle, K.W. Chou, A. Amassian, E.H. Sargent, Nat. Nanotechnol. 7 (2012) 577–582.
[39] Z.-K. Yuan, S. Chen, H. Xiang, X.-G. Gong, A. Walsh, J.-S. Park, I. Repins, S.-H. Wei, Adv. Funct. Mater. 25 (2015) 6733–6743.
[40] M. He, X. Zhang, J. Huang, J. Li, C. Yan, J. Kim, Y.-S. Chen, L. Yang, J.M. Cairney, Y. Zhang, S. Chen, J. Kim, M.A. Green, X. Hao, Adv. Energy Mater. 11 (2021), 2003783.
[41] T. Walter, R. Herberholz, C. Müller, H.W. Schock, J. Appl. Phys. 80 (1996) 4411–4420.
[42] P.D. Antunez, D.M. Bishop, Y. Luo, R. Haight, Nat. Energy 2 (2017) 884–890.

Zhuoran Wang, received his PhD in the department of Mining and Materials Engineering from the McGill University, QC, Canada in 2017. In 2019 he joined the Institute of Photonic Sciences (ICFO), Barcelona, as a postdoctoral research fellow. He is currently awarded by Marie-Curie Individual Fellowship to develop environmentally friendly thin film semiconductor for sustainable solar cell technologies.

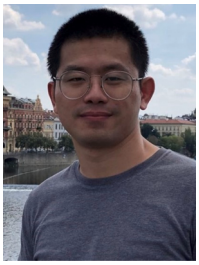

Yongjie Wang is a Ph.D student in the Institute of Photonic Sciences (ICFO), Barcelona, Spain. He graduated from Institute of Functional Nano & Soft Materials (FUNSOM), Soochow University with a master degree in Physics. His research is mainly focused on solution processed nanocrystals for energy harvesting and solar cells.

Gerasimos Konstantatos, received his PhD in the department of Electrical and Computer Engineering from the University of Toronto, ON, Canada in 2008. In 2009 he joined ICFO as an assistant Professor and since 2015 he is an ICREA research Professor at ICFO leading the Functional Optoelectronic Nanomaterials Group. His interests lie in developing solution processed nanomaterials, quantum dots and 2D materials for optoelectronic and solar cell applications. He is the recipient of MIT TR35 Spain award in 2012 and Fresnel Prize in 2013 for his salient contributions in the field of colloidal quantum dot optoelectronics.